

# Dynamics of magnetic nanoparticle suspensions

Vanchna Singh<sup>1</sup>, Varsha Banerjee<sup>1</sup> and Manish Sharma<sup>2</sup>

<sup>1</sup>*Department of Physics, Indian Institute of Technology,*

*Hauz Khas, New Delhi 110016, INDIA.*

<sup>2</sup>*Centre for Applied Research in Electronics,*

*Indian Institute of Technology, Hauz Khas, New Delhi 110016, INDIA.*

## Abstract

We study the dynamics of a suspension of magnetic nanoparticles. Their relaxation times are strongly size-dependent. The dominant mode of relaxation is also governed by the size of the particles. As a result the dynamics is greatly altered due to polydispersity in the sample. We study the effect of polydispersity on the response functions. These exhibit significant changes as the parameters characterizing polydispersity are varied. We also provide a procedure to extract the particle size distribution in a polydisperse sample using Cole-Cole plots. Further the presence of attractive interactions causes aggregation of particles leading to the formation of clusters. Repulsive interactions along with thermal disorder not only hinder aggregation, but also introduce the possibility of removal of particles or “fragmentation” from clusters. The competing mechanisms of aggregation and fragmentation yield a distribution of cluster sizes in the steady-state. We attempt to understand the formation of clusters and their distributions using a model incorporating the phenomena of aggregation and fragmentation. Scaling forms for quantities of interest have been obtained. Finally we compare our numerical results with experimental data. These comparisons are satisfactory.

PACS numbers: 47.57.E-,47.65.Cb,47.57.eb,89.75Da

## I. INTRODUCTION

Single domain magnetic nanoparticles (MNP) and their colloidal suspensions have attracted a lot of attention in the recent years [1]-[4]. The growing interest is due to a variety of technological applications associated with them. These range from mechanical and thermal applications involving their usage as sealants, lubricants and coolants to challenging applications in medicine for the purpose of magnetic resonance imaging, targeted drug delivery and biomarkers and biosensors to name a few. The main reason behind their wide applicability is the ease with which they can be detected and manipulated by the application of an external magnetic field. Their response times are strongly size-dependent, thus introducing the possibility of synthesizing particles to yield application tailored response times.

Most practical applications require appropriate surfactant coatings to prevent agglomeration and sedimentation of magnetic nanoparticles. Many biological and medical applications require nanoparticles with biologically relevant coatings in order to use them as probes and carriers [4, 5]. Such coatings enhance the particle size, although the magnetic volume remains unchanged. The Neel and Brownian relaxation times which characterize the dynamics of the suspension depend not only upon the constituting material, but also the magnetic volume and the enhanced volume due to surfactant coating. The interplay of these parameters governs whether one or both relaxation times contribute to the dynamics [1]-[3],[7]. In the present paper, we systematically analyze the effect of the above parameters on the relaxation times. We also study the ac susceptibility  $\chi(\omega)$ , the most commonly studied response function, in various regimes characterized by the relative dominance of the two relaxation times. This understanding makes it possible to estimate relaxation times as well as related parameters from the measurement of  $\chi(\omega)$  in the laboratory.

All experimental samples have a distribution of particle sizes and are referred to as polydisperse. The particle size distributions in experimental samples, usually obtained by a tunnelling electron microscopy (TEM) analysis, are found to have a log-normal form [1, 8]. Hence we incorporate the effect of polydispersity in our calculations of  $\chi(\omega)$ . As the Neel and Brownian relaxation times have a strong dependence on particle size, polydispersity leads to a considerable broadening and sometimes an additional peak in  $\chi''(\omega)$ . We have also worked out a procedure to obtain particle size distributions from the susceptibility data

via Cole-Cole plots when they are unavailable [10, 11].

The above approach assumes the *single particle model* [7] applicable to dilute suspensions in which magnetic interactions amongst particles may be ignored. Many biological applications are particularly benefitted by this approach. For instance diagnostic tools such as magnetic resonance imaging rely on transport and manipulation of individual magnetic particles bound by fluorescent dyes through blood vessels [12]. However many mechanical and thermal applications rely on viscosity effects arising due to a higher density of MNP in the suspensions. When present in sufficient concentration, clustering and chaining of MNP is rather common as observed by electron microscopy or dynamic light scattering studies [13]-[15]. This behavior is undesirable in many applications using magnetic fluids as sealants, coolants, lubricants, printing inks, etc. where invariance of the magnetic and fluid properties are paramount [1]. On the other hand magnetic domain detection, optical shutters, tagging of surfaces and other entities benefit from clustering of MNP [1, 16]. It is hence useful to understand the mechanisms responsible for clustering and the dependence of cluster-size distributions and average cluster sizes on the parameters describing the experimental sample. With this knowledge, it may be possible to synthesize application tailored suspensions.

Aggregation results due to a variety of interaction energies which come into play in magnetic suspension [1, 2, 17]. Typically these are dipolar, van der Waal and steric interactions. Of these the former two are attractive while the later is repulsive. Their relative strengths are governed by the magnetic compound, the magnetic volume, the thickness of the surfactant coating as well as the properties of the suspending liquid. Additionally, temperature acts as a disordering agent which can not only hinder aggregation but also introduce the possibility of detachment of the basic unit(s) from the parent cluster. Thus we expect the cluster-size distribution and average cluster size to be governed by the interplay of the attractive and repulsive forces amongst the interacting particles and the ambient temperature of the suspension.

Earlier models addressing the issue of clustering in MNP suspensions have treated aggregation as an irreversible mechanism. These models obtain a power law growth for the average cluster size in the initial stages of aggregation while the steady-state is characterized by a single cluster comprising of all the particles in the suspension [19]-[22]. The later is often referred to as an infinite cluster. We further add fragmentation in the model to counter irreversible aggregation, due to the presence of repulsive interactions and temperature. The

two competing mechanisms make cluster formation a self-limiting process resulting in a distribution of clusters of varying sizes with the average cluster size governed by the ratio  $R$  of the aggregation and fragmentation rates. We obtain the steady-state cluster-size distributions and the evolution of the mean cluster size to its steady-state value for different values of  $R$ . Both these functions exhibit scaling. We have compared our results with sets of experimental data to lend credence to our interpretations and observations of the aggregation-fragmentation model. These comparisons are much to our satisfaction.

The paper is organized as follows. Section II deals with relaxation mechanisms and response functions of dilute MNP suspensions using the single particle model. In Section II A, we introduce the Neel and Brownian relaxation times and identify regimes where either or both relaxation times contribute. Polydispersity and its characterization is introduced in Section II B. The calculation of the ac susceptibility  $\chi(\omega)$  for monodisperse and polydisperse samples in the different regimes described above is presented in Section II C. In Section II D, we provide a procedure to obtain particle-size distributions (for polydisperse samples) using Cole-Cole plots obtained from  $\chi(\omega)$ . Section III deals with aspects of clustering occurring in samples which are no longer governed by the single particle approximation. Interactions prevalent in samples exhibiting these phenomena are introduced in Section III A. We introduce the aggregation-fragmentation model to describe clustering in Section III B. The numerical results are presented in Section III C. Their comparisons with corresponding measurements in a variety of experimental systems are presented in Section III D. Finally we conclude this paper with a summary and discussion in Section IV.

## II. RELAXATION MECHANISMS AND RESPONSE FUNCTIONS OF DILUTE MNP SUSPENSIONS

We now study the relaxation properties and the response functions in dilute MNP suspensions where inter-particle interactions can be ignored. In this regime the particles essentially behave as independent, single-domain, super paramagnetic entities.

### A. Neel and Brownian relaxation times

A ferromagnetic sample such as iron for instance, has no net magnetization even below the Curie temperature. This is so because the sample comprises of domains, each having spontaneous magnetization pointing in a different direction. However if the size of the body is reduced, there comes a point beyond which the magnetostatic energy and the energy for forming domain walls compete in such a way that a single domain state becomes preferable [23]. The direction of magnetization of the single domain particle does not remain fixed in time though, but undergoes fluctuations or “relaxations” as the magnetic moment rotates between the crystallographic anisotropy axes. As a result the time averaged magnetization is still zero and the particle is still paramagnetic. It is called “super paramagnetic” because each particle has a giant magnetic moment arising due to a large number ( $\sim 10^5$ ) of individual atomic moments. We now describe the mechanisms of relaxation of these single domain super paramagnetic particles suspended in a liquid.

The magnetization vector of a single domain particle is given by [23]:

$$M = VM_o\hat{n}, \quad (1)$$

where  $V = 4\pi r_c^3/3$  is the magnetic volume of a particle with radius  $r_c$  usually referred to as the core radius,  $M_o$  is the saturation magnetization and  $\hat{n}$  a unit vector in the direction of the magnetization. In the case of uniaxial anisotropy (in the z-direction say), the magnetic energy is given by

$$E = VK \sin^2 \theta, \quad (2)$$

where  $K$  is the effective magnetic anisotropy constant and  $\theta$  is the angle between the z-axis and  $\hat{n}$ . Minimum energy occurs at  $\theta = 0$  and  $\pi$  defining two equilibrium orientations corresponding to magnetizations  $+VM_o$  and  $-VM_o$ . If thermal fluctuations are strong enough, magnetic moment reversal takes place within the particle by overcoming the energy barrier (of height  $VK$ ). This reversal or switching time is called Neel relaxation time and is given by

$$\tau_N = \tau_o e^{VK/k_B T}, \quad (3)$$

where  $\tau_o$  is related to the inverse of the attempt frequency of magnetic reversal.

There is another mechanism by which the magnetic moment of a super paramagnetic particle suspended in a fluid can relax. This mechanism of relaxation can be due to the

physical rotation of the particle within the fluid. It is referred to as Brownian rotational motion as it occurs due to the thermal fluctuations in the suspended medium. The Brownian relaxation time is given by [3]

$$\tau_B = \frac{4\pi\eta r_h^3}{k_B T}, \quad (4)$$

where  $\eta$  is the dynamic viscosity of carrier liquid and  $r_h$  is the hydrodynamic radius defined as the sum of the core radius  $r_c$  of the MNP and the surfactant coating  $\delta$  over it.

As can be seen from Eqs.(3) and (4), both Neel and Brownian relaxation times are highly sensitive to the particle size. While  $\tau_N$  increases exponentially,  $\tau_B$  grows linearly with the particle dimension. It is customary to define an effective relaxation time as follows [7, 8]:

$$\begin{aligned} \frac{1}{\tau_e} &= \frac{1}{\tau_N} + \frac{1}{\tau_B} \quad \text{or} \\ \tau_e &= \frac{\tau_N + \tau_B}{\tau_N \tau_B}. \end{aligned} \quad (5)$$

Thus it is possible to tailor time scales by an appropriate choice of parameters, particularly  $K$ ,  $r_c$  and  $r_h$ . With this in mind, we have systematically studied the effect of  $r_c$  and  $r_h$  on  $\tau_N$  and  $\tau_B$  and consequently  $\tau_e$  for maghemite ( $Fe_3O_4$ ) particles used most commonly in making magnetic fluids.

In Table I, we summarize our evaluations of  $\tau_N$ ,  $\tau_B$  and  $\tau_e$  for particles with varying magnetic core radius  $r_c$  and the thickness of the surfactant coating  $\delta$ . In most experiments, the later is usually in the range of 2-6 *nm*. As is observed in Table I,  $\tau_B$  is practically unaffected by  $\delta$ . For small particles,  $\tau_N \ll \tau_B$  which results in  $\tau_e \approx \tau_N$ . The relaxation then takes place by rotation of the magnetic moment inside the particle. For large particles on the other hand,  $\tau_B \ll \tau_N$ . Consequently  $\tau_e \approx \tau_B$  and the relaxation is due to a physical rotation of the particle in the suspension. Thus the choice of the relaxation mode is primarily governed by the particle size. For critical particle sizes, often called the cross-over radius  $r^*$  ( $\sim 8$  *nm* in Table I), it is found that both mechanisms contribute to the relaxation of the suspended particle.

We have studied the effect of temperature  $T$ , the surfactant coating  $\delta$  and the anisotropy constant  $K$  on the cross-over radius  $r^*$ . Most applications require an operating temperature in the range of 270 to 320 *K*. We find that  $r^*$  does not change perceptibly in this range. Further, as seen from Table I the variation of  $\delta$  does not significantly alter  $r^*$ . The anisotropy constant  $K$  on the other hand, leads to a substantial change in the corresponding value of

the cross-over radius. In Figure 1, we plot  $r^*$  as a function of the anisotropy constant  $K$  for a few frequently used biological and commercial spherical, magnetic nanoparticles. In all these evaluations, the temperature is assumed to be 300  $K$  and the surfactant coating  $\delta$  has been taken to be 2  $nm$ . The figure indicates that the value of the cross-over radius  $r^*$  is smaller for larger values of anisotropy  $K$ . Thus amongst the three parameters of relevance, the anisotropy constant  $K$  affects the cross-over radius  $r^*$  the most.

## B. Polydispersity

Monodisperse samples are an idealization. A variation in the particle size is inherent in all experimental samples. TEM studies of several samples have revealed a log-normal distribution for the variation of particle sizes [1, 8, 26]. Thus the probability density  $P(r_c)dr_c$  of having particles within radius  $r_c$  and  $r_c + dr_c$  can be written as:

$$P(r_c)dr_c = \frac{1}{\sqrt{2\pi \ln \sigma}} \exp \left[ -\ln^2(r_c/\bar{r}_c)/(2 \ln^2 \sigma) \right] dr_c, \quad (6)$$

where  $\bar{r}_c$  and  $\sigma$  are the mean and variance of the distribution. Due to the strong dependence of both Neel and Brownian relaxation times on particle size, it is evident that a distribution of relaxation times will be obtained if the suspended particles have a distribution of sizes. The presence of polydispersity leads to a significant change in the behavior of the response function of the sample as we shall see in the following subsection.

## C. A C susceptibility measurements

The complex susceptibility  $\chi(\omega)$  of a suspension of monodisperse MNP in the linear response regime has the Debye form given by [23]:

$$\chi(\omega) = \frac{\chi_o}{(1 - i\omega\tau_e)} \quad (7)$$

where  $\chi_o = \chi(\omega = 0) = NV^2M_o^2/k_B T$  is the static susceptibility of the sample comprising of  $N$  monodisperse particles of volume  $V$  with a saturation magnetization  $M_o$ . The effective relaxation time  $\tau_e$  is defined by Eq. (5). An experimental time scale is provided by  $\omega^{-1}$ , the inverse of the frequency of the applied oscillatory field. If  $\omega\tau_e \ll 1$ , the response is given by the static susceptibility  $\chi_o$  bearing the characteristic  $T^{-1}$  dependence. On the other hand,

if the two time scales are comparable, i.e. when  $\omega\tau_e \approx 1$ , the response is marked by strong frequency dependent effects. Separating the real and the imaginary parts of susceptibility yields:

$$\chi'(\omega) = \chi_o \frac{1}{1 + \omega^2\tau_e^2} \quad \text{and} \quad (8)$$

$$\chi''(\omega) = \chi_o \frac{\omega\tau_e}{1 + \omega^2\tau_e^2}. \quad (9)$$

The imaginary part of the susceptibility,  $\chi''(\omega)$  governs dissipation in the system. When plotted as a function of the frequency, it exhibits a symmetric peak around  $\omega = \tau_e^{-1}$ . Alternatively, the peak frequency can provide information about the radius  $r_c$  as well as the hydrodynamic radius  $r_h$  of the particle as will be discussed shortly.

The susceptibility response gets substantially altered in the presence of polydispersity. For polydisperse samples,  $\chi''(\omega)$  needs to be averaged over the particle size distribution  $P(r_c)$ . Thus

$$\chi'(\omega) = \chi_o \int dr_c P(r_c) \frac{1}{1 + \omega^2\tau_e^2(r_c)} \quad \text{and} \quad (10)$$

$$\chi''(\omega) = \chi_o \int dr_c P(r_c) \frac{\omega\tau_e(r_c)}{1 + \omega^2\tau_e^2(r_c)}. \quad (11)$$

In Figure 2, we plot Eq. (9) (open circles) for monodisperse samples corresponding to three different values of  $r_c = 4, 8$  and  $12 \text{ nm}$ . The chosen values correspond to (a)  $r_c < r^*$ , (b)  $r_c \approx r^*$  and (c)  $r_c > r^*$  respectively for maghemite particles used to generate data of Table I. All cases exhibit the characteristic Debye form. To understand the effect of polydispersity, we also plot Eq. (11) (filled circles) in the same figure. The distribution  $P(r_c)$  vs.  $r_c$  used for the evaluations were obtained from a TEM analysis of maghemite samples used in reference [8]. These distributions had a log-normal form with a variance  $\sigma \approx 0.35$ . The mean value  $\bar{r}_c$  is the particle size of the corresponding monodisperse evaluation.

As seen in Figure 2, a broadening of the response function is observed in all cases after the inclusion of polydispersity. The response no longer has the symmetric Debye form. In Figure 2a, the peak frequency provides information about the mean core radius  $\bar{r}_c$ . The width of the log-normal distribution often gives rise to a small Brownian peak although  $\bar{r}_c < r^*$  and the particles predominantly exhibit Neel relaxation. A pronounced two-peak response is obtained in Figure 2b since  $\bar{r}_c \approx r^*$ . Both Neel and Brownian relaxation contribute in this regime. The frequencies corresponding to the peak values yield information about



the average values of core and the hydrodynamic radii  $\bar{r}_c$  and  $\bar{r}_h$  of the particles. Finally when  $\bar{r}_c > r^*$ , the Brownian relaxation dominates and the frequency corresponding to the peak provides information regarding the hydrodynamic radius  $\bar{r}_h$  of the particle. Comparing Figures 2a and 2c, it is clear that polydispersity affects Neel relaxation more significantly than Brownian relaxation as expected (cf. Eqs. (3) and (4)).

#### D. Particle size distributions from Cole-Cole plots

The information on distribution of relaxation times can be obtained from susceptibility measurements by empirical models. The most frequently used model for obtaining the distribution of relaxation times is the Cole-Cole model. Based on this model, the dynamic susceptibility  $\chi(\omega)$  with multiple relaxation times is given by [10, 11]:

$$\chi(\omega) = \frac{\chi_o}{1 + (i\omega\tau_c)^{1-\alpha}}, \quad (12)$$

where  $\tau_c$  is the central relaxation time about which all the other relaxation times are distributed and  $\alpha$  is a fitting parameter with limits  $0 \leq \alpha \leq 1$ . The equation reduces to the Debye equation for  $\alpha=0$ . As the deviation from the single relaxation time model becomes greater,  $\alpha \rightarrow 1$ . Separating the real and imaginary parts of Eq.(12), we obtain:

$$\chi'(\omega) = \frac{\chi_o}{2} \left( 1 - \frac{\sinh(1-\alpha)s}{\cosh(1-\alpha)s + \cos(\alpha\pi/2)} \right) \quad \text{and} \quad (13)$$

$$\chi''(\omega) = \frac{\chi_o}{2} \frac{\cos(\alpha\pi/2)}{\cosh(1-\alpha)s + \sin(\alpha\pi/2)}, \quad (14)$$

where  $s = \log \omega\tau_c$ .

Cole and Cole proposed a method of graphically representing the effects of multiple relaxation times. The method consists of plotting  $\chi''(\omega)$  for a certain frequency against  $\chi'(\omega)$  at the same frequency. These are called Cole-Cole plots. When  $\alpha = 0$ , the Cole-Cole plot is a semi-circle. When  $\alpha > 0$ , the Cole-Cole plot is still a semi-circular arc similar to a widened Debye curve, but in this case the centre lies below the horizontal axis. The plot is symmetrical about the vertical line passing through the point  $\chi'(\omega) = \chi_o/2$  when  $\chi''(\omega)$  is maximum at a frequency  $\omega = \tau_c^{-1}$ . The parameter  $\alpha$  can be determined from the Cole-Cole plot by a graphical construction. We do not reiterate this rather well established procedure here, but refer the reader to reference [10] for it. It may also be determined by best fits of Eq. (13) and Eq. (14) to the experimental data. It should be noted that the

symmetrical distribution of relaxation times is a consequence of a particle size distribution which is symmetric about the mean value  $\bar{r}_c$ . The Cole-Cole model assumes a gaussian form for  $P(r_c)$  vs.  $r_c$ . The parameter  $\alpha$  is hence related to the spread of the gaussian distribution with  $\alpha = 0$  yielding a delta function or a monodisperse particle size distribution.

The response functions in typical MNP suspensions, as observed from Figure 2, are asymmetrical primarily due to the log-normal particle size distributions. The Cole-Cole model is thus not the most suitable for their description. Experimental systems exhibiting asymmetric response functions can be conveniently represented by an expression due to Cole and Davidson. The ac susceptibility in this model is given by [27]:

$$\chi(\omega) = \frac{\chi_c}{(1 + i\omega\tau_c)^\beta}, \quad (15)$$

where  $0 \leq \beta \leq 1$  and is related to the deviation from the single relaxation time model. The Debye form of Eq. (7) is recovered when  $\beta = 1$ . Separating the real and imaginary parts of Eq. (15) results in:

$$\chi'(\omega) = \chi_o \cos \phi^\beta \cos \beta \phi \quad \text{and} \quad (16)$$

$$\chi''(\omega) = \chi_o \cos \phi^\beta \sin \beta \phi, \quad (17)$$

where  $\phi = \arctan \omega\tau_c$ . Eqs. (16) and (17) give rise to a “skewed arc” in the Cole-Cole plots. The parameter  $\beta$  can be obtained by a graphical construction or by fitting the experimental data corresponding to  $\chi'(\omega)$  and  $\chi''(\omega)$  with Eqs. (16)-(17).

In Figure 3 we show the Cole-Cole plots for the same polydisperse samples that were used to obtain data of Figure 2. The cases (a), (b) and (c) correspond to  $\bar{r}_c < r^*$ ,  $\bar{r}_c \approx r^*$  and  $\bar{r}_c > r^*$  respectively. In all the three cases, the centre of the arc lies below the horizontal axis due to multiple relaxation times resulting from polydispersity. Further, the asymmetry in the particle size distributions is reflected in the asymmetry of the arcs. The Cole-Cole plots are distinct in each of the regimes. In particular, the cross-over regime is characterized by a two-humped form signifying a comparable contribution of both Neel and Brownian relaxation to the response function. Thus significant information regarding the experimental sample can be inferred from the Cole-Cole plots.

We now provide a simple procedure for evaluating the particle-size distribution  $P(r_c)$  vs.  $r_c$  in the experimental sample when the response function exhibits multiple relaxation times. Assuming a log-normal form,  $P(r_c)$  vs.  $r_c$  is characterized by its mean  $\bar{r}_c$  and

variance  $\sigma$  signifying the spread in the particle-size distributions. While the evaluation of  $\bar{r}_c$  is straightforward, the variance  $\sigma$  needs to be estimated. Recalling that multiple relaxation times are a consequence of polydispersity, it is imperative to connect  $\beta$  with  $\sigma$ . In order to find this relationship, we have gone through the following sequence of steps. Firstly  $\chi'(\omega)$  and  $\chi''(\omega)$  were evaluated using Eqs. (10) and (11) for a chosen value of  $\bar{r}_c$  and  $\sigma$ . The corresponding values of  $\tau_c$  and  $\beta$  were then obtained by fitting the above susceptibility data with Eqs. (16) and (17) of the Cole-Davidson model. This procedure was then repeated for a number of  $\sigma$  values in the range 0.1 to 0.5, keeping  $\bar{r}_c$  constant. Larger values of  $\sigma$  were not considered as they resulted in extremely broad log-normal distributions which are not of relevance in experiments. The above evaluation was then performed for three different values of  $K$ . The results obtained are plotted in Figure 4 on a semi-logarithmic scale. The solid lines follow the equation:

$$\sigma = A(K)e^{-B\beta}. \quad (18)$$

The parameters  $A(K)$  and  $B$  in each case are obtained from the best fits of the above equation to the evaluated data. We find that  $B = 2.45 \pm 0.05$  and is independent of  $K$ . We also find that Eq. (18) and the parameter  $B$  is unaffected by  $\bar{r}_c$ , which was varied from 4 to 12 nm.

We test the procedure for extracting particle-size distribution from the susceptibility data on maghemite nanoparticle suspensions provided in reference [8]. From the Cole-Cole plots of this data, we evaluated the best-fit values of  $\tau_c$  and  $\beta$ . These were found to be  $2 \times 10^{-8}$  s and 0.44 respectively. The average core radius  $\bar{r}_c$ , evaluated from  $\tau_c$  using Eq. (3), was found to be 4.2 nm. The value of  $\sigma$  characterizing the spread of the log-normal distribution was then obtained using Eq. (18) and was found to be 0.36. The reconstructed particle-size distribution is shown in Figure 5. The particle-size distribution obtained using TEM measurements has also been provided in the figure for comparisons. In general, we find that this procedure reproduces the original distributions rather well when the response function has one dominant peak, be it in the Neel or the Brownian relaxation regime.

### III. CLUSTERING IN MNP SUSPENSIONS

The properties of the magnetic fluid are greatly affected by the aggregation of particles (inspite of surfactant coating) due to the presence of attractive and repulsive interactions.

It is hence instructive to consider the different interaction energies in MNP suspensions and understand their interplay which leads to the formation of aggregates or clusters of different sizes.

### A. Interactions in MNP suspensions

The primary interaction energies in these systems are enumerated below [1]:

#### 1. Dipolar interaction:

As each particle is magnetized, the attractive dipole-dipole interaction could in principle force particle agglomeration. The dipolar interaction energy between two magnetic nanoparticles, each having a magnetic moment  $\mu$  is given by:

$$E_d(s) = -\frac{\mu_o}{4\pi} \left( \frac{3\mu \cdot (\mu \cdot \vec{s})\vec{s}}{s^5} - \frac{\mu^2}{s^3} \right), \quad (19)$$

where  $s$  is the center-to-center separation between the two nanoparticles and the permeability of free space  $\mu_o = 4\pi \times 10^{-7} \text{ Hm}^{-1}$ . As the magnetic properties of the particles are affected by temperature, the dipolar interaction defined above is also temperature dependent.

#### 2. van der Waal's interaction:

It arises spontaneously between neutral particles because of the fluctuating electric dipolar forces and is attractive in nature. Hamaker calculated this interaction for identical spheres separated by a surface-to-surface distance  $l$  to be:

$$E_v = \frac{A}{6} \left\{ \frac{2}{l^2 + 4l} + \frac{2}{(l+2)^2} + \ln \left( \frac{l^2 + 4l}{l^2 + 4l + 4} \right) \right\}. \quad (20)$$

In the above equation, the Hamaker constant  $A = 10^{-19} \text{ Nm}$ . It should be noted that the  $l^{-1}$  dependence in the above equation indicates that infinite energy is required to separate a particle pair while a finite energy is required in its formation. Therefore agglomeration of particles will occur as long as the Hamaker constant has a finite value. As a result van der Waal's interaction unlike dipolar interaction is unaffected by temperature.

#### 3. Steric interaction:

The steric energy comes into play due to the presence of long chained surfactant

molecules coating the particles. This mechanism prevents the particles from approaching very close to one another, thus preventing the van der Waal's attraction to come into play. This repulsive interaction originates due to a compression of the surface-adsorbed surfactant molecules when the inter particle separation is smaller than two times the thickness of the surfactant layer. For a sufficient density of the surfactant layer, the repulsion can grow large enough to avoid the contact between the magnetic particles. This repulsive energy for spherical particles has been calculated by Papell and is given by the following form:

$$E_s = \frac{E}{1.325} \left(2\delta - \frac{s}{2}\right)^{\frac{5}{2}} \left(\frac{d_c}{2} + \delta\right)^{\frac{1}{2}}. \quad (21)$$

In the above form, the Young's modulus  $E$  was assumed to be  $10^6$  and  $d_c = 2r_c$  is the diameter of the magnetic core of the particle.

Apart from the above interaction energies, the thermal energy responsible for the Brownian motion of the suspended particles also plays an important role in the aggregation dynamics. An appropriate value of temperature (which depends on the size of the interacting particles) is capable of preventing aggregation. In principle, this condition may be expressed as a comparison between the attractive energy with the thermal energy of the two particles which yields a numerical value of the core radius  $r_c$  at which this could happen. We expect the thermal degrees of freedom, in conjunction with steric repulsion, to not only hamper the aggregation process but also remove particles from the parent cluster leading to its fragmentation.

At this juncture we define a parameter  $\Omega$  as the ratio of energies leading to aggregation to those which lead to fragmentation follows:

$$\Omega = \frac{E_d + E_v}{E_s + k_B T}. \quad (22)$$

It is expected that the distribution of cluster sizes and the mean cluster size will be governed by the ratio  $\Omega$ . In the following subsection, we present a model which incorporates the competing mechanisms of aggregation and fragmentation.

## B. The aggregation-fragmentation model

The formulation introduced by Smoluchowski is especially useful to model a suspension of magnetic nanoparticles [19]. To begin with, we assume that the suspension contains  $N$  identical, single particles executing Brownian motion. The later leads to aggregation of two particles if they come within an appropriate range of one another and the net interaction between them is attractive. The resulting cluster of size two also executes Brownian motion, but with a reduced diffusion rate till it encounters a particle or a cluster of particles. The process goes on and eventually a single large cluster comprising of all the  $N$  particles is formed. Such a cluster is usually referred to as an infinite aggregate. In most useful suspensions however there is a distribution of clusters of varying sizes. As discussed in the preceding subsection, the combined effects of thermal energy and inter-particle repulsion can introduce fragmentation in the cluster dynamics thereby preventing the formation of large aggregates. We thus include this additional mechanism in the rate equations which describe the evolution of clusters.

Let  $c(k, t)$  denote the number of clusters containing  $k$  particles at time  $t$ . The time evolution of  $c(k, t)$  is governed by the following rate equations:

$$\begin{aligned} \frac{\partial c(k, t)}{\partial t} = & \frac{1}{2} \sum_{i+j=k} K_{ij} c(i, t) c(j, t) - c(k, t) \sum_{j=1}^{\infty} K_{kj} c(j, t) \\ & + f_{k+1} c(k+1, t) - f_k c(k, t) + \delta_{k,1} \sum_{j=1}^{\infty} f_j c(j, t), \quad k \geq 1. \end{aligned} \quad (23)$$

In the above equation the  $K_{ij}$  and  $f_k$  are the aggregation and fragmentation kernels respectively whose forms are specified below. The aggregation kernel describes the coalescence of a cluster containing  $i$  particles with another containing  $j$  particles to yield a larger aggregate comprising of  $k = i + j$  particles. It is assumed to have a mass-dependent form defined by  $K_{ij} = D(i^{-\mu} + j^{-\mu})$  to take into account the reduced mobility of large clusters. A value of  $\mu = 0$  implies a mass-independent mobility, i.e., clusters of all sizes diffuse with the same ease. A non-zero values of  $\mu$  results in a slower mobility of larger clusters and consequently a slower growth rate of clusters. In the limit of  $\mu = \infty$ , only monomers are mobile. The choice of  $\mu$  is dictated by the experimental parameters as we shall see in a short while. The fragmentation kernel  $f_k$  describes the loss of a particle from the parent cluster and can also be assumed to have a mass-dependent form defined by  $f_k = \omega k^\nu$ . In our studies however,

we have set  $\nu = 0$  to reduce the number of parameters in the model. The parameters  $D$  and  $\omega$  define the relative strength of the aggregation and fragmentation processes.

The first and the third term in Eq.(23) are referred to as the gain terms which result in the formation of clusters of size  $k$ . The former describes aggregation of two clusters to yield a cluster containing  $k$  particles while the later describes the generation of a cluster comprising of  $k$  particles due to fragmentation of a particle from a cluster of size  $k + 1$ . The second and the fourth term on the other hand are referred to as the loss terms which describe processes leading to loss of clusters of size  $k$ . This could be due to aggregation of a cluster of size  $k$  with another or the its fragmentation. The fifth term in the equation describes the generation of single particles from clusters due to the process of fragmentation. It is easy to check that the following sum rule is satisfied:

$$\frac{\partial}{\partial t} \left( \sum_{k=1}^{\infty} k c(k, t) \right) = 0, \quad \text{or} \quad \sum_{k=1}^{\infty} k c(k, t) = N, \quad (24)$$

as required by conservation conditions.

The condition  $\partial c(k, t)/\partial t = 0$  describes the steady-state which is of interest to us. In the absence of the fragmentation term, Eq.(23) reduces to the Smoluchowski equation describing coagulation phenomena [19]. There have been a few studies of this model, both analytical and numerical, to predict scaling forms associated with cluster growth and cluster-size distributions [20]-[22],[28]-[31]. The growth of clusters with time is a power governed by the relation  $\langle k(t) \rangle \sim t^z$ . Choosing  $\mu = 1$ , the value of  $z$  was estimated to be  $\simeq 0.5$ . The steady state in this model was found to be an infinite (single) aggregate comprising of all the  $N$  particles. Note that in the absence of fragmentation, the constant  $D$  can be absorbed by redefining  $t$  as  $Dt$  in Eq. (23), making the later independent of the aggregation rate.

To mimic those physical situations which do not have an infinite-aggregate as a steady-state but rather have a distribution of clusters of varying sizes, it is essential to include fragmentation as a competing mechanism to aggregation. Of relevance in the context of the present study is model incorporating mass-independent aggregation and mass-dependent evaporation processes reported in reference [29]. The competition between aggregation and evaporation leads to several asymptotic outcomes of the steady-state solution of this model. For instance if evaporation dominates over aggregation, the steady-state cluster size distribution  $c(k)$  vs.  $k$  decays exponentially. On the other hand for a critical evaporation rate, the distribution decays as  $k^{-5/2}$ .

It is convenient to rewrite Eq.(23) in terms of  $P(k, t)$ , the probability of having cluster of size  $k$  at time  $t$ . Defining the later as  $P(k, t) = c(k, t) / \sum_{k=1}^{\infty} c(k, t)$ , its evolution is governed by the following equation:

$$\begin{aligned} \frac{\partial P(k, t)}{\partial t} = & \sum_{i+j=k} K_{ij} P(i, t)P(j, t) - P(k, t) \sum_{j=1}^{\infty} K_{kj} P(j, t) \\ & + \omega P(k+1, t) - \omega P(k, t), \quad k > 1, \end{aligned} \quad (25)$$

$$\frac{\partial P(1, t)}{\partial t} = -P(1, t) \sum_{j=1}^{\infty} K_{kj} P(j, t) + \omega \sum_{j=2}^{\infty} P(j, t), \quad k = 1. \quad (26)$$

The above equations also satisfy the sum rule

$$\frac{\partial}{\partial t} \left( \sum_{k=1}^{\infty} P(k, t) \right) = 0, \quad \text{or} \quad \sum_{k=1}^{\infty} P(k, t) = 1, \quad (27)$$

as required.

### C. Numerical results

We now solve the the set of equations defined by Eqs. (25)-(26) numerically to obtain the steady-state cluster size distribution  $P(k)$  vs.  $k$ . It is useful to define the ratio  $R$  characterizing the relative strengths the aggregation and fragmentation mechanisms:

$$R = \frac{D}{\omega}. \quad (28)$$

Identifying the physical origin of  $D$  in the attractive interactions between clusters and that of  $\omega$  in the disordering agents (such as repulsive interactions and temperature), we can expect  $R$  to have the same qualitative effect as the ratio  $\Omega$  defined in Eq. (22) on steady-state cluster size distributions. We use this correspondence to bring contact between numerical results and experimental observations on cluster formation in MNP suspensions.

In Figure 6a, we look at the variation of the mean cluster size  $\langle k(R, t) \rangle$  as a function of  $t$  for different values of  $R$  on a double logarithmic scale. The parameter  $\mu$  was chosen to be 2.0. After an initial growth period obeying a power law, the cluster size attains a steady-state value of  $\langle k(R) \rangle$  due to the competing mechanisms of aggregation and fragmentation. As expected,  $\langle k(R) \rangle$  increases with increasing values of  $R$ . In fact we find that  $\langle k(R) \rangle \sim R^\alpha$  with  $\alpha = 0.85 \pm 0.02$  as can be seen in the inset. Further, in the diffusion domiated regime ( $R \gtrsim 0.5$ ) the data in Figure 6a can be scaled by replotting  $\langle k(R, t) \rangle / \langle k(R) \rangle$



vs.  $t/t_s$  where  $t_s$  is the time taken to attain the steady-state. The initial cluster growth is of the form  $\langle k(t) \rangle \sim t^z$ . We find that the growth exponent  $z = 0.38 \pm 0.02$ . The scaled data is shown in Figure 6b on a double logarithmic scale. The best fit line with a slope of 0.38 is also indicated. The value of the growth exponent also depends upon the value of  $\mu$ . For  $\mu = 1.0$ , our simulations yield  $z = 0.78 \pm 0.02$ . The corresponding scaled data and the power law fit is also shown in the inset of Figure 6b. The faster growth of clusters is a consequence of increased mobility due to a lower value of  $\mu$ .

Next in Figure 7a we plot the steady-state distribution  $P(k)$  vs.  $k$  corresponding to  $\mu = 2$  for the same set of  $R$  values considered above. We find that the tails of the distributions fit well to a power law in  $k$ . In Figure 7b, we plot  $\langle k(R) \rangle P(k)$  vs.  $k/\langle k(R) \rangle$  where  $\langle k(R) \rangle$  is the steady-state average cluster size for the corresponding value of  $R$ . These plots indicate that the distribution functions  $P(k)$  corresponding to different values of  $R$  obey scaling in the diffusion-dominated regime. The scaling relation can be summarized in the following equation:

$$P(k) = \frac{1}{\langle k(R) \rangle} f\left(\frac{k}{\langle k(R) \rangle}\right), \quad \langle k(R) \rangle \sim R^\alpha. \quad (29)$$

#### D. Comparisons with experimental data

We now compare our simulation results with experimental data on average cluster sizes in a variety of magnetic nanoparticle suspensions. Eberbeck, et al studied the aggregation of various magnetic nanoparticles in a variety of media such as water, phosphate buffered saline, calf serum, bovine serum and human serum [17, 32]. The experimental measurements were performed at room temperature. In all cases, formation of dimers and trimers were reported by the authors. To make comparisons with the simulation results of our model, we first calculate the ratio  $\Omega$  defined in Eq.(22) for each of the samples. These along with the sample specifications are tabulated in Table II. As can be seen in column 4,  $\Omega$  is in the range 0.35 to 0.70. Referring to the plot of  $\langle k(R) \rangle$  vs.  $R$  for  $\mu = 2$  in the inset of Figure 6a, a value of  $R$  in the above range yields dimers and trimers in the steady-state.

Next we look at experiments which report the formation of long chains of magnetic nanoparticles in the presence of an applied magnetic field  $H$ . The particles acquire dipole moment  $\tilde{\mu}$  given by:

$$\tilde{\mu} = \frac{4}{3}\pi r_c^3 \mu_o \chi H, \quad (30)$$

where  $r_c$  is the core radius of the magnetic particle and  $\chi$  is the magnetic susceptibility. The interaction energy between two particles with aligned, identical dipole moments is given by:

$$U(s, \theta) = \frac{\mu^2}{4\pi\mu_o} \frac{1 - 3\cos^2\theta}{s^3}, \quad (31)$$

where  $s$  is the centre to centre separation between the two particles and  $\theta$  is the angle between the applied field and the line joining the centres of the spherical particles. The interaction is thus attractive when the dipoles are head-to-tail and repulsive when they are side-by-side. For these samples, the dominant interaction is dipolar. Thus the parameter  $\Omega$  defined in Eq. (22) reduces to

$$\Omega_H = \frac{\pi r_c^3 \mu_o \chi^2 H^2}{9k_B T}, \quad (32)$$

where we have assumed the dipolar interaction to be at its maximum, when the particles are aligned with the external field. In the presence of an external field, if the resulting magnetic dipole-dipole interaction between particles exceeds the thermal energy, then the particles arrange themselves into chains which are column-like for low volume fractions and worm-like structures for high-volume fraction [13, 14]. Many theoretical studies on the above systems have been based on Smoluchowski kinetic equations for irreversible aggregation [20, 21].

A set of experimental measurements which we find especially relevant in the context of the aggregation-fragmentation model are reported in reference [13]. In this paper, the authors have studied aggregation dynamics in very dilute emulsions of ferrofluid droplets in water. The ferrofluid droplets were small  $Fe_3O_4$  grains in kerosene coated with a surfactant to prevent agglomeration. The data on average chain lengths as a function of time for different volume fractions and applied fields was obtained using dynamic light scattering experiments. We reproduce a scaled form of this data in Figure 8. On the x-axis, we plot  $t/t_s$  where  $t_s$  is the time taken to reach the steady-state value of the average cluster. The y-axis has been scaled by the steady-state value of the average chain length. The unscaled data is also provided in the inset for reference. As can be observed in Figure 8, the scaled form (as well as the unscaled form) of the experimental data bears a qualitative resemblance to Figure 6b which results from the numerical solution of the aggregation-fragmentation model defined by Eqs. (25) and (26). The slow initial growth, the power law form at intermediate times and saturation to a steady-state value as time progresses are borne by both sets of data.

On the quantitative side, we find that the experimental data is well represented by a growth exponent  $z = 0.78 \pm 0.02$  obtained with  $\mu = 1$  in our simulations. The corresponding

line is depicted in figure 8. It is pertinent to recall here that the dipolar interaction becomes dominant in the presence of the applied magnetic field thereby increasing the diffusivity of the clusters. In the aggregation-fragmentation model, the later can be achieved by an increase in the value  $D$  as well as a decrease in the value of  $\mu$ . Consequently, we find that our data on  $\langle k(R, t) \rangle$  vs.  $t$  for a value of  $\mu = 1$  rather than  $\mu = 2$  results in accurate comparisons with experimental data. The initial growth does not conform to the predicted value of  $z = 0.5$  (also obtained with  $\mu = 1$ ) of the irreversible aggregation model.

A similar set of experimental results were obtained in reference [14] where the power law prediction for cluster growth was checked by performing a large number of experiments on aqueous solutions of super paramagnetic polystyrene beads having a uniform distribution of  $Fe_3O_4$  particles. The data was obtained for five values of the volume fraction in the presence of low field strengths and higher field strength using optical microscopy. The exponent  $z$  describing the cluster growth in these studies was found to be much larger than the predicted value of 0.5 especially for small volume fractions and low field strengths. These observations further reiterate the appropriateness of introducing fragmentation along with aggregation especially in the above limits where the thermal energy plays a significant role in the dynamics.

#### IV. SUMMARY AND DISCUSSION

We conclude this paper with a summary of results and discussion presented here. Our main interest was to understand the factors governing the dynamical response of suspensions of single-domain magnetic nanoparticles. Such an understanding introduces the possibility of synthesizing particles with application tailored response times. The effect of sample parameters on the Neel and Brownian relaxation times which characterize the response was studied. Amongst all the parameters of relevance, the anisotropy of the constituting material and the particle size alter the relaxation time most significantly. Infact the dominant relaxation time is also decided primarily by the particle size. We also studied how these parameters affect the ac susceptibility  $\chi(\omega)$  which is the most commonly studied response function in the laboratory. This understanding proves to be useful in estimating relaxation times as well as sample parameters from the measurement of  $\chi(\omega)$  in the laboratory.

We have then studied the effect of polydispersity, an inherent feature of all samples on the

response characteristics. These exhibit significant changes due to the strong dependence of relaxation times on particle sizes. The primary effect is the broadening of response functions and in some cases the later exhibits a two peaked structure. We have also worked out a procedure to obtain the particle-size distribution from  $\chi(\omega)$  using Cole-Cole plots and the analysis of Cole and Davidson. This provides an alternative approach to TEM analysis which is usually employed to obtain particle-size distributions.

The above studies assumed a single-particle model applicable to dilute suspensions. However in many cases the inter-particle interactions cannot be ignored. Clustering of particles is inevitable in such suspensions. While the formation of clusters is undesirable in some applications, it is beneficial in many others. Hence we have tried to understand the mechanisms responsible for clustering and the experimental parameters which govern the properties of cluster-size distribution and the average cluster size. This knowledge is useful for the synthesis of application tailored suspensions.

A model incorporating the phenomena of aggregation and fragmentation was used to understand aspects of clustering. The steady-state cluster size distributions of the model were obtained by numerically solving the rate equations describing the evolution of clusters. We have obtained scaling forms for the cluster-size distributions and the average cluster size. Our results agree well with experiments where clustering or chain formation have been observed.

**Acknowledgment** VS and VB would like to acknowledge the support of CSIR Grant No. 03(1077)/06/EMR-II. VB would also like to acknowledge the hospitality of ICTP, Italy where part of the work was completed.

- 
- [1] Rosensweig R E 1997 *Ferrohydrodynamics* (New York: Dover).
- [2] Odenbach S 2002 *Magnetoviscous effects in ferrofluids* (Berlin: Springer Verlag)
- [3] Coffey W T, Kalmykov Yu P and Waldron J T 1996 *The Langevin Equation* (Singapore: World Scientific)
- [4] Pankhurst Q A, Connolly J, Jones S K and Dobson J 2003 *J.Phys.D: Appl.Phys.* **36** R167
- [5] Astalan A P, Ahrentrop F, Johansson C, Larsson K and Krozer A 2004 *Biosensors and Bioelectronics* **19** 945
- [6] Chung S, Hoffmann A and Bader S A 2004 *Appl. Phys. Lett.* **85** 2971
- [7] Shliomis M I and Raikher Y 1980 *IEEE Mag.* **16** 237
- [8] Fannin P C and Charles S W 1989 *J. Phys. D: Appl. Phys.* **22** 187
- [9] Rinaldi C, Chaves A, Elborai S, He X and Zahn M 2005 *Current Opinion in Colloid and Interface Sciences* **10** 141
- [10] Cole K S and Cole R H 1941 *J. Chem. Phys.* **9** 341
- [11] Cole K S and Cole R H 1942 *J. Chem. Phys.* **10** 98
- [12] Zhao M, Kircher M F, Josephson L and Weissleder R 2002 *Bio. Conjug. Chem.* **13** 840
- [13] Promislow J H E, Gast A P and Fermigier M 1995 *J. Chem. Phys.* **102** 5492
- [14] Hagenbuchle M and Liu J 1997 *Appl. Optics* **36** 7664
- [15] Kellner R R and Kohler W 2005 *J. Appl. Phys.* **97** 034910
- [16] Hasmonay E and Depeyrot J 2000 *J. Appl. Phys.* **88** 6628
- [17] Eberbeck D, Wiekhorst F, Steinhoff U and Trahms L 2006 *J. Phys.: Condens. Matter* **18** S2829
- [18] Smoluchowski M V 1916 *Z.Phys.* **17** 585
- [19] Chandrasekhar S 1943 *Stochastic Problems in Physics and Astronomy, Rev. Mod. Phys.* **15** 1
- [20] Miyazima S, Meakin P and Family F 1987 *Phys. Rev. A* **36** 1421
- [21] Kandel D 1997 *Phys. Rev. Lett.* **79** 4238
- [22] Morimoto H and Maekawa T 2000 *J. Phys. A: Math. Gen.* **33** 247
- [23] Dattagupta S 1987 *Relaxation Phenomena in Condensed Matter Physics* (Orlando: Academic Press)
- [24] Brown W F 1963 *J. Appl. Phys.* **34** 1319

- [25] Chikazumi S 1997 *Physics of Ferromagnetism* (New York: Oxford University Press )
- [26] Fannin P C, Relihan T and Charles S W 1997 *Phys.Rev B* **55** 14423
- [27] Davidson D W and Cole R H 1951 *J. Chem. Phys.* **19** 1484
- [28] Ernst M H and Dongen P G J 1987 *Phys. Rev. A* **36** 435
- [29] Krapivsky P L and Redner S 1996 *Phys. Rev. E* **54** 3553
- [30] Chavez F, Moreau M and Vicente L 1997 *J. Phys. A.: Math. Gen.* **30** 6615
- [31] Kalachev L, Morimoto H and Maekawa T 2001 *Int. J. Mod. Phys. B* **15** 774
- [32] Eberbeck D, Bergemann C, Hartwig S, Steinhoff U and Trahms L 2005 *J. Magn. Magn. Mater.* **289** 435

## Figure Captions

**Table I:** Variation of the Neel ( $\tau_N$ ), Brownian ( $\tau_B$ ) and effective ( $\tau_e$ ) relaxation times as a function of the core radius  $r_c$  of the magnetic nanoparticle.  $\tau_B$  has also been evaluated for three values of the surfactant coating  $\delta$ . The corresponding  $\tau_e$  for these values is also evaluated.

**Table II:** Calculated value of the ratio  $\eta$  and the corresponding estimated value of the cluster size for a variety of MNP used in experiments by Eberbeck, et al [17, 32]. The experimental parameters associated with each sample are also specified.

**Figure 1:** Variation of the cross-over radius  $r^*$  as a function of the anisotropy constant  $K$  for several biologically and commercially used magnetic nanoparticles. The surfactant coating  $\delta$  and the temperature  $T$  were taken to be 2 nm and 300 K respectively in these evaluations.

**Figure 2:** Variation of  $\chi''(\omega)$  vs.  $\omega$  for monodisperse (open circles) and polydisperse (filled circles) maghemite samples when (a)  $\bar{r}_c < r^*$  and Neel relaxation dominates, (b)  $\bar{r}_c \approx r^*$  and both Neel and Brownian relaxation contribute and (c)  $\bar{r}_c > r^*$  and Brownian relaxation dominates. The values of  $\bar{r}_c$  in (a), (b) and (c) have been chosen as 4, 8 and 12 nm respectively. The surfactant coating  $\delta$  and the temperature  $T$  were taken to be 2 nm and 300 K respectively in these evaluations.

**Figure 3:** Cole-Cole plots (open circles) for data of figure 2 when (a)  $\bar{r}_c < r^*$  and Neel relaxation dominates, (b)  $\bar{r}_c \approx r^*$  and both Neel and Brownian relaxation contribute and (c)  $\bar{r}_c > r^*$  and Brownian relaxation dominates. The plots exhibit a two-humped structure when both relaxation times contribute (case b). The  $\beta$  and the  $\tau_c$  values obtained from the Cole-Davidson equations (refer text in section II C) are also indicated in the figures.

**Figure 4:** Variation of  $\sigma$  as a function of  $\beta$  for three different anisotropy constants on a semi-logarithmic scale.

**Figure 5:** The reconstructed particle size distribution along with the particle size distribution obtained using TEM for comparisons (refer text in section II D for details).

**Figure 6:** (a) Variation of the mean cluster size  $\langle k(R, t) \rangle$  as a function of time  $t$  for  $\mu = 2$  and different values of the ratio  $R$  specified in the figure. The inset shows the steady-state value of the mean cluster size  $\langle k(R) \rangle$  as a function of  $R$  on a double logarithmic scale. The best fit line to data has a slope  $0.85 \pm 0.02$  respectively. (b) Scaled data of (a) with the scaled axes as indicated in the figure. The initial growth of clusters obeys a power law characterized by the exponent  $z = 0.38 \pm 0.02$ . Similar data corresponding to  $\mu = 1$  is also indicated in the inset. For this data, the growth exponent  $z = 0.78 \pm 0.02$  as indicated.

**Figure 7:** (a) Steady-state distribution  $P(k)$ . vs  $k$  for  $\mu = 2$  for indicated values of ratio  $R$ . (b) Scaled data of (a) with the scaled axis as indicated in the figure.

**Figure 8:** Data from reference [13] on average chain length as a function of time for different volume fractions replotted on scaled axes as shown in the figure. The solid line corresponds to a slope of 0.78 obtained from a numerical solution of the aggregation-fragmentation model with  $\mu = 1$  (refer inset of figure 6b and corresponding text).



**Table I**

$r_c$ (nm)	$\tau_N$ (s)	$\tau_B$ (s)			$\tau_e$ (s)		
	(s)	$\delta_1=2$ nm	$\delta_2=4$ nm	$\delta_3=6$ nm	$\tau_{e1}$	$\tau_{e2}$	$\tau_{e3}$
4	$10^{-9}$	$10^{-7}$	$10^{-6}$	$10^{-6}$	$10^{-9}$	$10^{-9}$	$10^{-9}$
6	$10^{-8}$	$10^{-6}$	$10^{-6}$	$10^{-6}$	$10^{-8}$	$10^{-8}$	$10^{-8}$
8	$10^{-5}$	$10^{-6}$	$10^{-6}$	$10^{-6}$	$10^{-6}$	$10^{-6}$	$10^{-6}$
10	$10^{-1}$	$10^{-6}$	$10^{-6}$	$10^{-5}$	$10^{-6}$	$10^{-6}$	$10^{-5}$
15	$10^{20}$	$10^{-5}$	$10^{-5}$	$10^{-5}$	$10^{-5}$	$10^{-5}$	$10^{-5}$
20	$10^{61}$	$10^{-5}$	$10^{-5}$	$10^{-5}$	$10^{-5}$	$10^{-5}$	$10^{-5}$

**Table II**

MNP Sample	Core	Shell	$\Omega$	$\langle k \rangle$
DDN128	$Fe_3O_4$	carboxydextran	0.5364	2.3
FluidMagD5	$Fe_3O_4$	starch	0.36	2.0
MagBSA	$Fe_3O_4$	BSA	0.676	2.5
Resovist	$Fe_3O_4$	Carboydextran	0.51	2.4

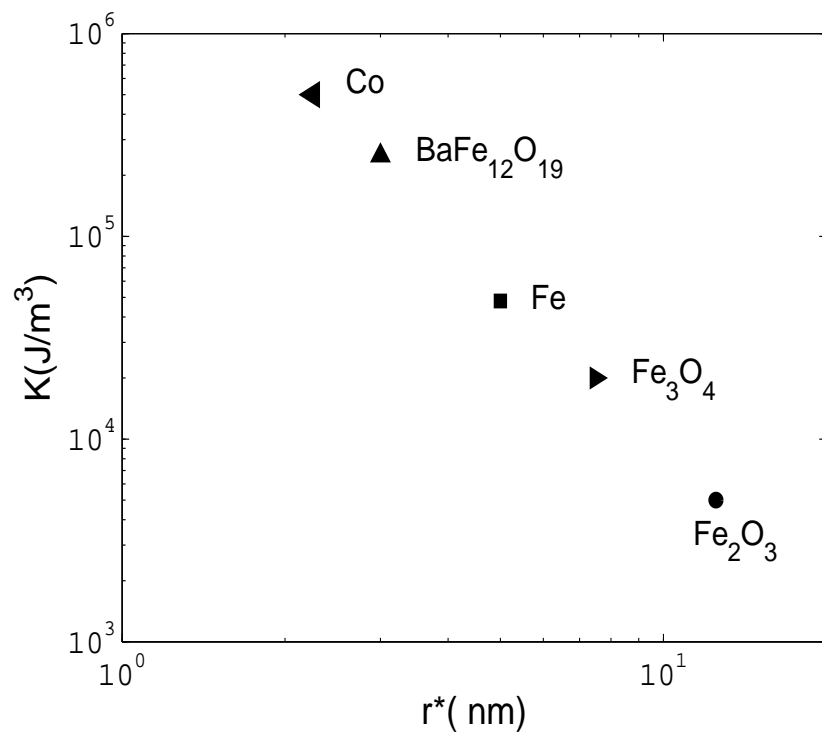


Figure 1

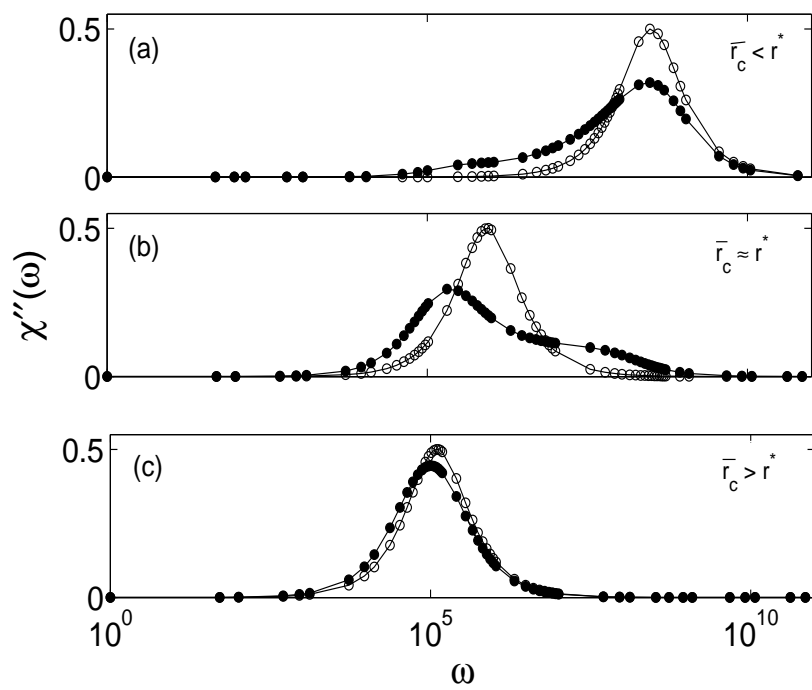


Figure 2

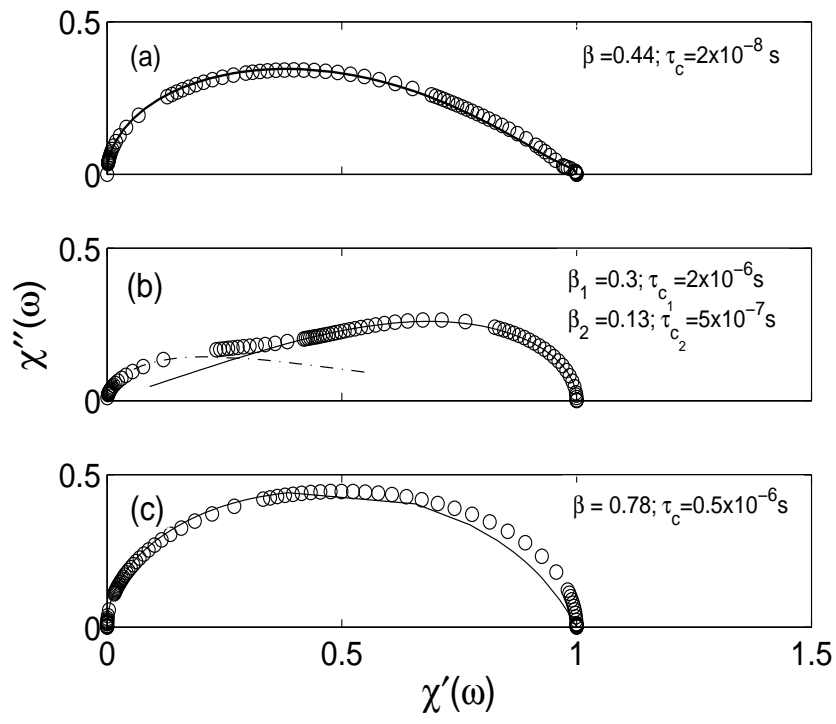


Figure 3

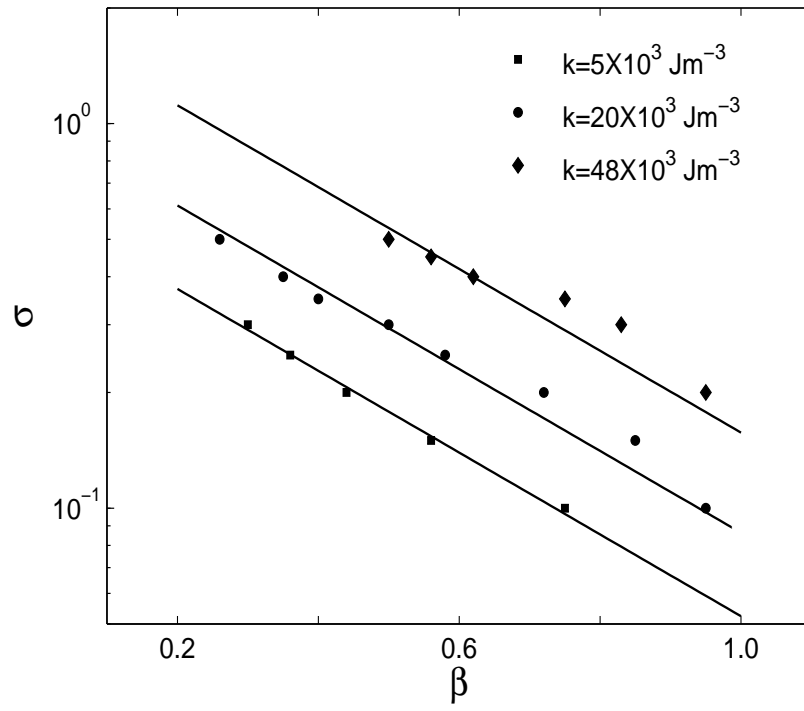


Figure 4

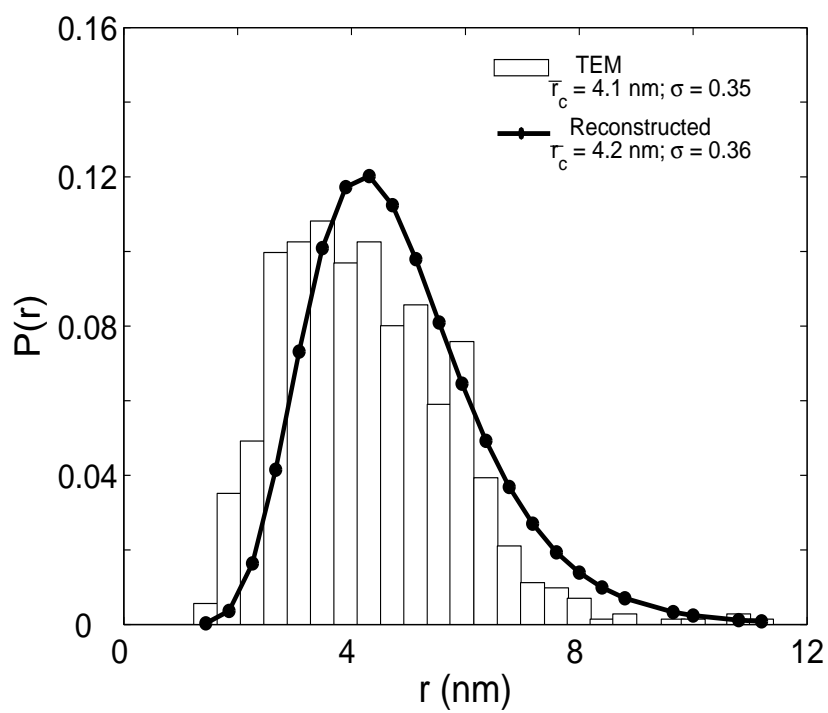


Figure 5

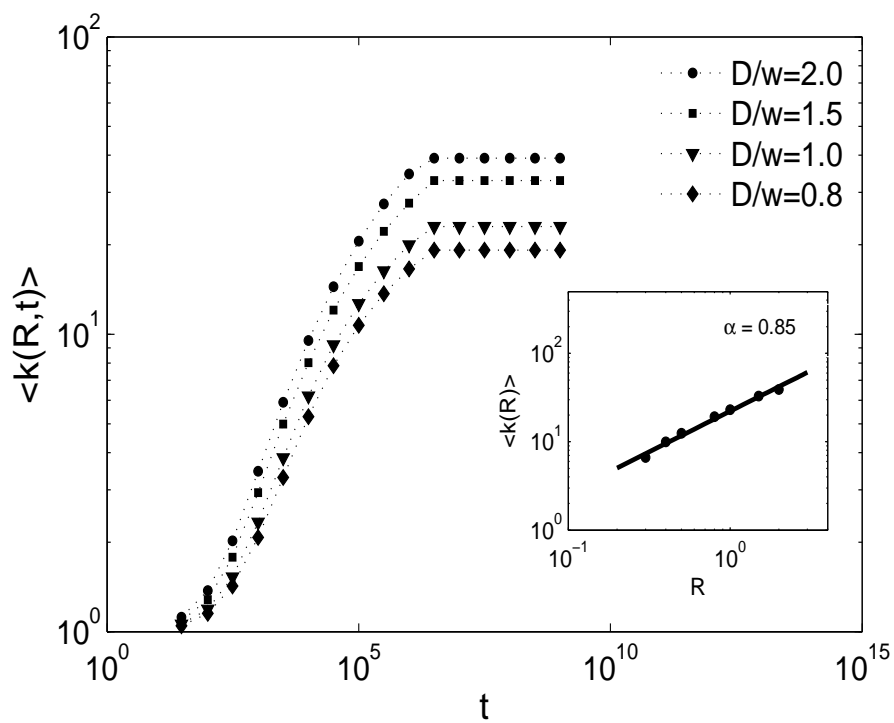


Figure 6a

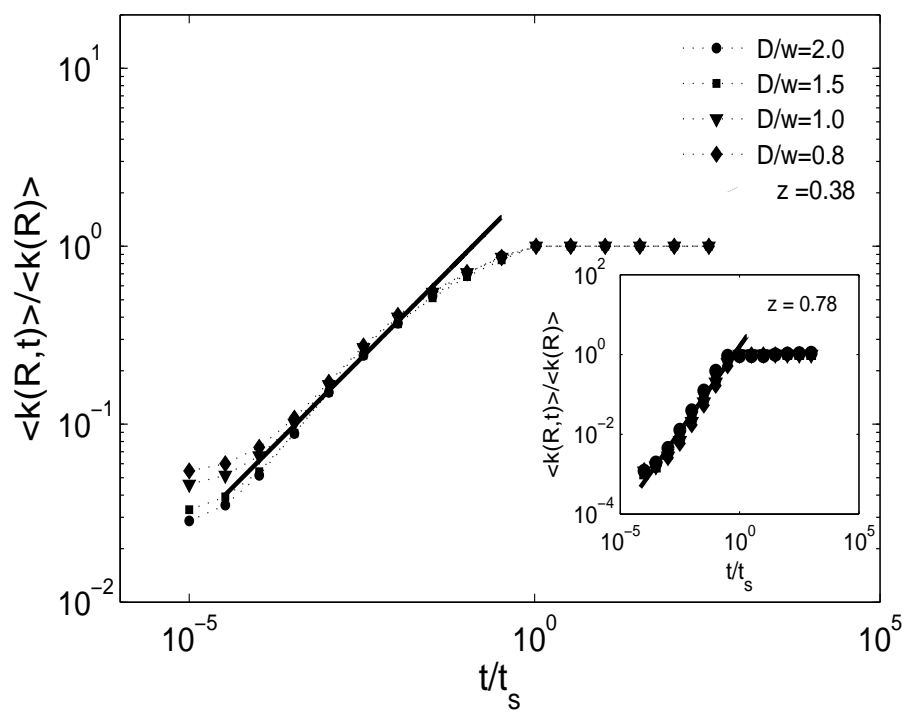


Figure 6b

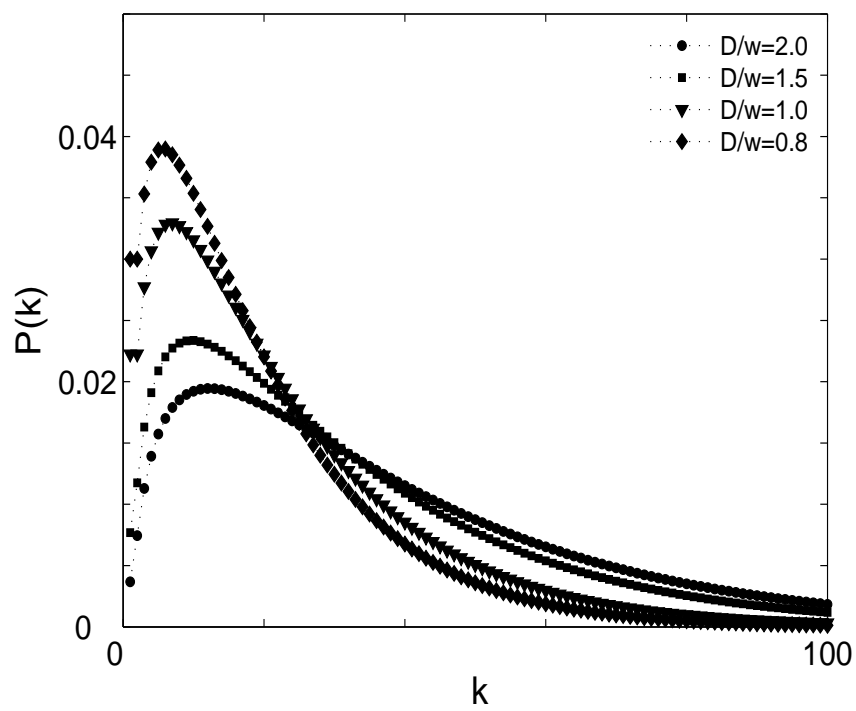


Figure 7a

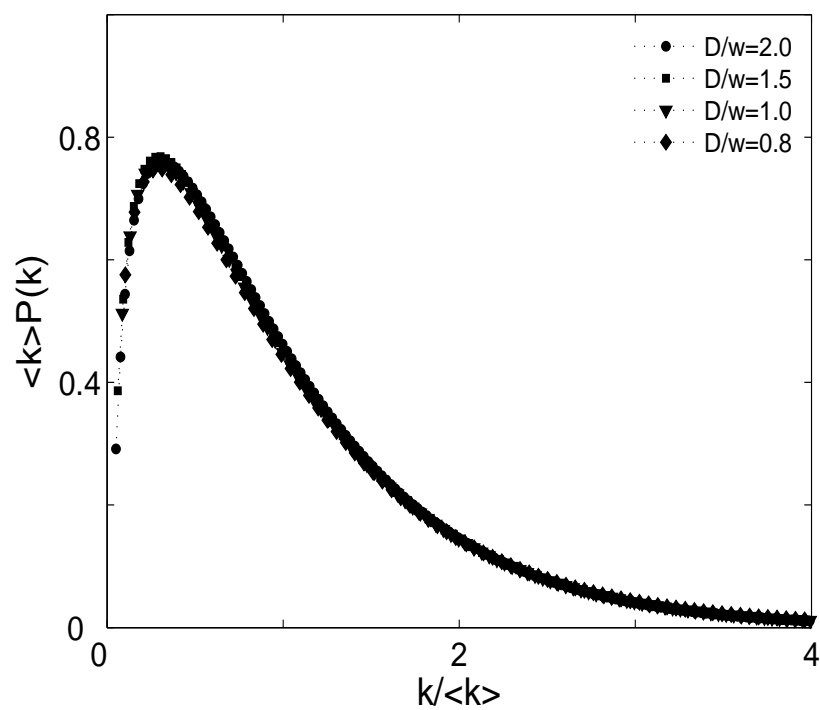


Figure 7b

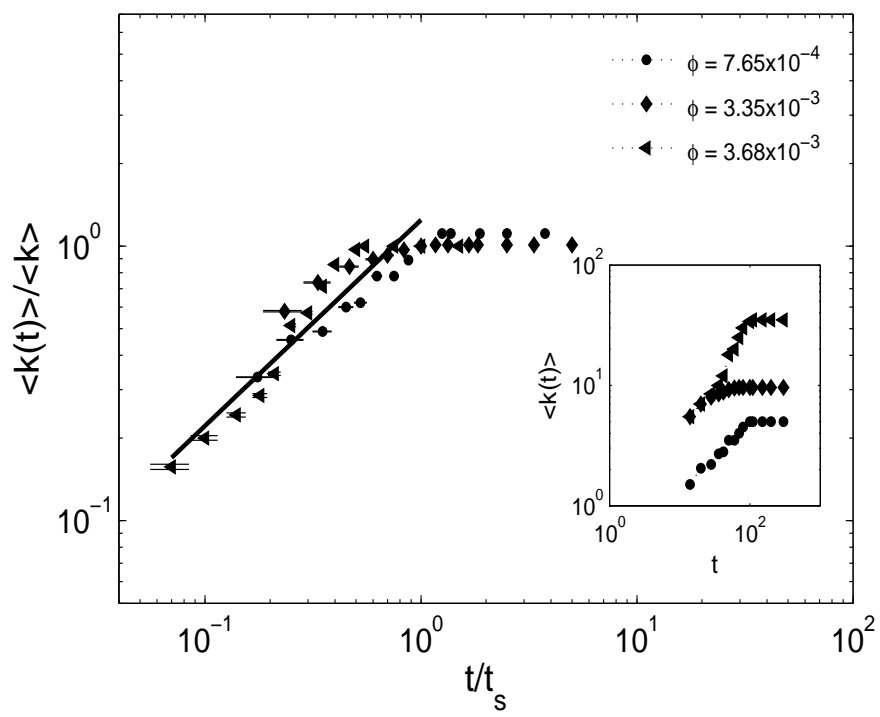


Figure 8